Effect of correlated oxide electrodes on disorder pinning and thermal roughening of ferroelectric domain walls in epitaxial math xmlns="http://www.w3.org/1998/Math/MathML">mrow>mi>Pb/mi>msub>mi>Zr/mi>mrow>mn>0.2/mn>/mrow>/msub>msub>mi>Ti/mi>mrow>mn>0.8/mn>/mrow>/msub>msub>mi mathvariant="normal">O/mi>mn>3/mn>/msub>/mrow>/math> thin films

Kun Wang, Yifei Hao, Le Zhang, Yuanyuan Zhang, Xuegang Chen, and Xia Hong

Phys. Rev. Materials **5**, 074402 — Published 9 July 2021

DOI: 10.1103/PhysRevMaterials.5.074402

Effect of Correlated Oxide Electrodes on Disorder Pinning and Thermal Roughening of Ferroelectric Domain Walls in Epitaxial $PbZr_{0.2}Ti_{0.8}O_3$ Thin Films

Kun Wang,[1] Yifei Hao,[1] Le Zhang,[1] Yuanyuan Zhang,[1] Xuegang Chen,[1] and Xia Hong[1,2]

[1] *Department of Physics and Astronomy, University of Nebraska-Lincoln, Nebraska 68588-0299, USA*

[2] *Nebraska Center for Materials and Nanoscience, University of Nebraska-Lincoln, Nebraska 68588-0299, USA*

Abstract

We report the competing effects of disorder pinning and thermal roughening on ferroelectric domain walls as a function of temperature in epitaxial $PbZr_{0.2}Ti_{0.8}O_3$ thin films deposited on (001) $SrTiO_3$ substrates buffered by three types of correlated oxide electrodes, $La_{0.67}Sr_{0.33}MnO_3$, $LaNiO_3$, and $SrIrO_3$. Piezo-response force microscopy studies show that the 50 nm $PbZr_{0.2}Ti_{0.8}O_3$ films are uniformly polarized in the as-grown states, with the patterned domain structures persisting up to 700 °C. For all three types of films, the domain wall roughness is dominated by 2D random bond disorder at room temperature, and transitions to 1D thermal roughening upon heating. The roughness exponent ζ increases progressively from 0.3 to 0.5 within a temperature window that depends on the bottom conducting oxide type, from which we extracted the distribution of disorder pinning energy. We discuss the possible origins of the disorder pinning and the effect of the correlated oxide electrodes on the energy landscape of DW motion.

I. Introduction

Domain walls (DW) in ferroelectric oxides play an important role in determining their dielectric properties and polarization switching dynamics. It has been shown that the presence of DW can lead to enhanced dielectric susceptibility and piezoelectric response [1]. As prototypical topological defects [2] with unusual conduction [3, 4], DWs can also be treated as individual functional entities for data storage [5]. The closure-type chiral dipole rotation at the DW surface has been utilized to tailor the nonlinear optical response [6, 7] and design van der Waals negative capacitance transistors [8]. When subjected to a small electric field, a DW goes through a nonlinear creep process that is governed by DW elasticity and disordered pinning [9]. Even without a bias field, DWs become mobile when the thermal energy exceeds the local disorder pinning [10]. The DW motion can affect the switching hysteresis and dielectric losses in ferroelectrics [11], which is critical for developing piezoelectric-based actuator and energy harvesting devices. Understanding the competing effects of the driving electric field, disorder pinning, and thermal activation on the nanoscale configuration of DWs thus has important implications in the functional design and device implementation of ferroelectrics.

Ferroelectric DWs can be modeled as elastic manifolds roughened in a disordered media [10, 12, 13]. The disorder pinning can be associated with the intrinsic defects in ferroelectric oxides, such as oxygen vacancies and cation disorders [14, 15], or be affected by the conducting electrodes through the build-in band misalignment [16, 17] or interfacial defect states [18-20]. The static configuration of DWs directly reflects the relative strength of disorder pinning and thermal fluctuation [21]. For epitaxial ferroelectric perovskite films, including Pb(Zr,Ti)O_3, $BaTiO_3$, and $BiFeO_3$, correlated oxides (CO) such as (La,Sr)MnO_3 are widely exploited as the conductive electrodes. The electrode layer can have significant impacts on the ferroelectric instability, as manifested in the finite size effect, modified Curie temperature T_C, and polarization asymmetry [22]. The ferroelectric/correlated oxide heterostructure is also a model system for examining interfacial magnetoelectric coupling [23] and polarization controlled quantum phase transitions [24], as well as developing multiferroic tunnel junctions [25] and ferroelectric field effect transistors [24]. Despite the intensive fundamental and technological interests in these hybrid systems, in-depth understanding of the effect of correlated oxides on the nanoscale configuration and thermal stability of ferroelectric domain structures is yet to be gained.

In this work, we report a comprehensive study of the effect of three types of correlated oxide electrodes on disorder pining and thermal roughening of DWs in epitaxial $PbZr_{0.2}Ti_{0.8}O_3$ (PZT) films. $La_{0.67}Sr_{0.33}MnO_3$ (LSMO), $LaNiO_3$ (LNO), and $SrIrO_3$ (SIO) were chosen as the electrode layers for their high metallicity and intriguing properties, such as colossal magnetoresistance [18, 24], strain and dimensionality-driven metal-insulator transition [26-28], and strong spin-orbit coupling [28]. Piezo-response force microscopy (PFM) measurements revealed strong polarization asymmetry and enhanced T_C exceeding 700 °C in these samples. Upon heating, the DW roughness evolves from two-dimensional (2D) random bond (RB) disorder-dominated behavior to one-dimensional (1D) thermal roughening. From the temperature dependence, we extracted the energy ranges of disorder pinning to be 63–82 meV, 36-47 meV, and 25-35 meV for PZT films on LSMO, LNO, and SIO, respectively. We discuss possible scenarios for the correlated oxide electrodes in modifying the energy landscape of DW motion, including interfacial clamping effect and polarization-specific accumulation of oxygen vacancies at the interface.

II. Sample Preparation and Experimental Method

We deposited 50 nm PZT films on (001) STO substrates buffered by 10 nm LSMO, LNO, and SIO using off-axis radio frequency magnetron sputtering [28, 29]. X-ray diffraction (XRD) scans reveal high-quality single crystalline (001) growth of all films (Supplemental Section 1) [30]. Atomic force microscopy (AFM, Bruker Multimode 8) studies show smooth film surfaces with root-mean-square roughness of $2-4$ Å [30]. For domain writing, a bias voltage (V_{bias}) larger than the coercive voltage was applied between the conductive Pt/Ir-coated probe (NanoSensors PPP-EFM) and the bottom correlated oxide [Fig. 1(a)]. Previous studies of epitaxial (001) PZT thin films showed that domain nucleation starts at one interface, which is followed by DW motion till it reaches the other interface, resulting in sharp 180° DWs [20, 31]. Domain imaging was conducted using PFM close to one of the cantilever's resonant frequencies (370±30 kHz). The initial images were taken after 24 hours of domain writing to eliminate artifacts due to charging [32]. The samples were then subjected to progressively higher temperatures, and the domain structures were imaged using both *in situ* PFM and the thermal-quench (TQ) method at room temperature (RT). The results reported here are based on three PZT/LSMO (denoted as S1, S2, and S3), one PZT/LNO, and two PZT/SIO samples (S1 and S2).

III. Piezoresponse Force Microscopy Studies

Figures 1(b)-(c) show the PFM switching hystereses taken on a PZT/LSMO sample (S1). The coercive voltage (V_c) is +5.5 V for the polarization down (P_{down}) state and -2.5 V for the polarization up (P_{up}) state, which is relatively high compared with those in PZT/LNO (+1.9 V/-2.8 V) and PZT/SIO (+1.8 V/-0.5 V) (Supplemental Fig. S4-S5) [30]. Figures 1(d)-(e) show the PFM phase and amplitude image of concentric square domains written on this sample. The as-grown film is uniformly polarized in the P_{up} state, indicating it is energetically more favorable. The PZT films deposited on LNO and SIO, on the other hand, prefer P_{down} and P_{up} polarization, respectively. The polarization asymmetry is consistent with the asymmetric V_c and commonly observed in epitaxial ferroelectric thin films, which can be attributed to the asymmetric electronic and mechanical boundary conditions.

Previous studies have shown that the static configuration of ferroelectric DWs contains important information of the system, including the dimensionality, nature of disorder, range of elastic interaction, and thermal fluctuation [13]. For a D-dimensional elastic media, DW can be treated as a $D-1$-dimensional interface separating different domain regions. The DW roughness can be characterized using the correlation function of the relative displacement between two points along the DW separated by a distance L: $B(L) = \overline{\langle [u(x+L) - u(x)]^2 \rangle}$, where $u(x)$ is the perpendicular displacement from a straight configuration at point x [Fig. 1(f) inset], and $\langle ... \rangle$ and $\overline{...}$ average $u(x)$ over the DW longitudinal coordinate and disorder, respectively. It has been shown by scaling theory that $B(L)$ follows a power-law dependence, $B(L) \propto L^{2\zeta}$, above the characteristic Larkin length L_C, which is on the order of DW width [12]. The roughness exponent ζ is determined by the collective contributions from the thermal- and disorder-roughening [10, 21]. The two universality classes of disorders that can affect DW roughness are the RB and random field (RF) disorders. The RB disorder locally modifies the ferroelectric double-well potential depth symmetrically, with ζ given by:

$$\zeta_{\mathrm{RB}} = \begin{cases} 2/3, & d_{\mathrm{eff}} = 1 \\ 0.2084(4 - d_{\mathrm{eff}}), & d_{\mathrm{eff}} > 1 \end{cases}. \tag{1}$$

Here d_{eff} is the effective dimensionality, which equals 1 for a 1D DW and 2.5 for a 2D DW in ferroelectrics [9, 33]. The additional $1/2$ for the latter originates from the long-range dipolar interactions, leading to $\zeta_{\mathrm{2D}} = 0.31$ [13]. The RF disorder prefers one polarization direction over the other, rendering an asymmetric double-well potential, with $\zeta_{\mathrm{RF}} = (4 - d_{\mathrm{eff}})/3$ for all dimensions. At high temperatures, thermal fluctuation becomes the dominating roughening mechanism. For 1D DW, the thermal roughness exponent is $\zeta_{\mathrm{TF}} = 1/2$ [10].

To extract ζ, we wrote sequentially P_{up} and P_{down} stripe domains to create six straight DWs on each sample (Fig. 2), and analyzed $B(L)$ for each DW from the PFM phase image to extract the roughness exponent ζ. The final ζ value was averaged over six DWs. Figure 1(f) shows the log-log plot of $B(L)$ taken on three types of PZT samples at RT. All samples exhibit a quasi-linear dependence at low L, which saturates above a characteristic length L_{sat} of about 50 nm. The quasi-linear region can be well described by a power exponent of $2\zeta = 0.62$, which corresponds to 2D RB disorder dominated behavior, consistent with previous studies of epitaxial PZT films at RT [9, 21]. For two points separated beyond L_{sat}, we consider their roughening no longer correlated elastically.

To study the thermal effect on the ferroelectric domain structures, we subjected the stripe domains to progressively higher temperatures, and performed PFM imaging using two methods. The *in situ* PFM imaging was carried out at elevated temperatures up to 200 °C using Bruker's TAC Thermal Application Controller System. For each temperature, *in situ* domain imaging was taken after the sample was heated on the AFM sample holder for 30 minutes at the stabilized temperature. In the thermal quench method, the sample was held at a stabilized temperature for 30 minutes in a muffle furnace, with heating operated in the non-overshooting mode. We then quenched the sample to RT by placing it on a metal plate to freeze the high-temperature domain structure [21, 34]. Both methods give highly consistent results.

Figure 2 shows the PFM phase images of the stripe domains taken at RT and after selected TQ cycles. For PZT on LSMO [Fig. 2(a)], the domain structures remain stable after TQ at 700 °C. At 650 °C, spontaneous polarization switching starts to occur as the thermal energy exceeds disorder pinning, resulting in scattered small bubble domains in the uniformly polarized regions. As the sample is further heated to 750 °C, the initial DWs become no longer recognizable, suggesting the sample is approaching T_C. Similar change in the domain structure has been observed in PZT on LNO [Fig. 2(b)] and SIO [Fig. 2(c)], where the spontaneous bubble domain formation occurs at around 650 °C and 600 °C, respectively. We denoted the lowest temperature at which the bubble domains were observed as T_{bubble}, as summarized in Table 1. For all three types of samples, T_C is well above 700 °C, much higher than the bulk value of ~460 °C. Such T_C enhancement has been widely observed in epitaxial PZT thin films [21]. It has been shown that the lattice distortion imposed by the substrate strain can modify the polarization terms of the Gibbs energy expansion, leading to an enhanced T_C [35].

In Fig. 3(a), we compared the $\zeta(T)$ data obtained on two PZT/LSMO samples up to 200 °C, which were taken with different methods. Both samples exhibit weak T-dependence in ζ, consistent with a 2D RB disorder interface. In contrast, for the samples on SIO, ζ increases steadily from 0.3 to 0.5 [Fig. 3(b)]. The highly reproducible results obtained on different samples using different methods confirm that the sharp difference in the T-dependence reflects the intrinsic characteristic behavior of the system. It also shows that the thermal roughening of DW at high temperatures can be preserved when the samples are quenched to RT, confirming that the TQ method is reliable for exploring the change of DW's configuration at high temperatures.

Figure 3(c) shows the $\zeta(T)$ data for all three types of samples using the TQ method. Above T_{bubble}, we have identified the DW regions that are free of the bubble domains to calculate ζ (Supplemental Section 4) [30]. The highest temperature we performed DW roughness analysis is 700 ºC, beyond which the DWs become highly perturbed by the bubble domains. All samples show 2D RB disorder dominated behavior at RT followed by a rapid increase of ζ within a characteristic temperature window. Out of this window the change in ζ is relatively weak. The two samples on LSMO exhibit highly consistent $\zeta(T)$, with ζ increasing from 0.3 to 0.5-0.6 between 500 °C and 675 °C. For PZT on LNO, the pronounced change in ζ occurs at a much lower temperature window between 150 °C and 275 °C. For PZT on SIO, a rapid increase in ζ starts even at RT and saturates at about 145 °C. For all samples, the critical change of ζ occurs below T_{bubble} (Table 1). This result clearly shows that even though all samples exhibit similarly enhanced T_{C} (above 700 °C), their DW pinning potential differ significantly.

From $\zeta(T)$, we identified two characteristic transition temperatures: T_{cr} marks where ζ starts to deviate rapidly from the 2D RB dominated behavior; T_{th} marks where ζ approaches the theoretical value of 1D thermal roughening $\zeta_{\mathrm{TF}} = 1/2$. The evolution from 2D to 1D dominated behavior is accompanied with the increasing L_{sat}, which characterizes the maximum separation between two points along the DW that can be viewed as elastically correlated. When temperature increases, DW gains thermal energy and becomes more mobile. L_{sat} progressively increases from 50 nm at RT to about 100 nm at T_{th} (Supplemental Section 3) [30]. As L_{sat} becomes much larger than the film thickness, the system can be viewed effectively as a 2D elastic system with 1D DW. Above T_{th}, ζ exhibits a very weak T-dependence and remains far below the theoretical value for 1D RB disorder $\zeta_{\mathrm{1D}} = 2/3$ up to T_{bubble}, indicating that the thermal roughening dominates disorder pinning in 1D systems.

IV. Discussion

a. Temperature-Dependence of DW Roughness

The T-dependence of DW roughness can be understood by considering the competing effects of disorder pinning and thermal fluctuation on DW motion. In Fig. 4(a), we modeled the local DW motion as a particle moving in a random pinning energy landscape $U_{\mathrm{RB}}(y)$, where the local energy barriers have the minimum barrier height of $U_{\mathrm{RB,min}}$ and maximum value of $U_{\mathrm{RB,max}}$. During DW writing, we applied a bias voltage V_{bias} to a conductive AFM tip, which tilted the local energy profile [Fig. 4(b)]. After the V_{bias} is removed, the particle (DW) becomes trapped, so the initial DW roughness can be viewed as a result of DW creep in a disorder modified energy landscape [12]. At elevated temperatures, the DW motion can be divided into three regimes: the low-temperature disorder-pinning regime (I), the intermediate temperature depinning regime (II), and the high-temperature thermal fluctuation regime (III) [Fig. 4(c)]. In regime I, the thermal energy is below $U_{\mathrm{RB,min}}$, and the DW roughness is dominated by the 2D RB disorder ($\zeta = \zeta_{\mathrm{RB}}$). In regime II, the thermal energy is between $U_{\mathrm{RB,min}}$ and $U_{\mathrm{RB,max}}$. The local DW trapped by the shallow wells with $U_{\mathrm{RB}}(y) < k_{\mathrm{B}}T$ can be activated and move to a neighboring meta-stable position, triggering the depinning process at some locations. As $B(L)$ is averaged over a large number of disorder sites, the extracted ζ value is between ζ_{2D} to ζ_{TF}, depending on the pinning energy distribution with respect to thermal fluctuation. With increasing temperature, local DWs trapped in a larger range of pinning potential gain sufficiently high thermal energy to overcome the energy barriers, and the roughness exponent increases progressively from ζ_{2D} to ζ_{TF}. Above T_{th} (regime III), $k_{\mathrm{B}}T > U_{\mathrm{RB,max}}$, so the entire DW is depinned, with ζ approaching ζ_{TF}. Upon rapid cooling, the local DWs become trapped in the local pinning energy minima, and the high-temperature DW configuration can be "frozen" during the thermal quench.

In this scenario, we can correlate the two transition temperatures with the strength of the disorder pinning energy: 1) $T_{\mathrm{cr}}(K) = U_{\mathrm{RB,min}}/k_{\mathrm{B}}$ is the first deflection point in $\zeta(T)$, where ζ starts to deviate rapidly from $\zeta_{\mathrm{2D}} = 0.31$; 2) $T_{\mathrm{th}}(K) = U_{\mathrm{RB,max}}/k_{\mathrm{B}}$ is the second deflection point, where ζ reaches $\zeta_{\mathrm{th}} = 0.5$. Here we converted the temperature unit to Kelvin. Figures 4(d)-(f) show the log-log plot of $\zeta(T)$ data for the PZT films on LSMO, LNO, and SIO, respectively, from which we identified T_{cr} and T_{th} and extracted the energy range of the characteristic disorder pinning potential, or $U_{\mathrm{RB,min}}$ and $U_{\mathrm{RB,max}}$.

	PZT/LSMO S1	PZT/LSMO S2	PZT/LNO	PZT/SIO S1
T_{cr} (°C)	497 ± 15	457 ± 15	147 ± 15	17 ± 15
T_{th} (°C)	677 ± 15	647 ± 15	277 ± 15	137 ± 15
T_{bubble} (°C)	675	650	650	600
$U_{\mathrm{RB,min}}$ (meV)	66 ± 2	63 ± 2	36 ± 2	25 ± 2
$U_{\mathrm{RB,max}}$ (meV)	82 ± 2	79 ± 2	47 ± 2	35 ± 2

ΔW (eV)	0.4 ± 0.2 [36]	0.7 ± 0.1 [37]	0.15 ± 0.1 [38]

Table 1. Summary of T_{cr}, T_{th}, T_{bubble}, energy range of disorder pinning, and work function mismatch ΔW between PZT and the electrode.

Table 1 summarizes the transition temperatures and the corresponding disorder pinning energy for all samples studied. The two PZT/LSMO samples show very similar T_{cr} and T_{th}, confirming the robustness of our method. The highest disorder pinning energy is observed in PZT/LSMO, while the DW in PZT/SIO is the least pinned. This trend is also consistent with that of coercive voltages observed in the three types of samples [Fig. 1(b)-(c) and Supplemental Section 2] [30]. It is thus expected that DWs in PZT/LSMO are the most thermally stable. As the DW remains to be relatively smooth (low ζ) over a wide temperature range, PZT/LSMO can also host the highest domain density, which is important for high density nonvolatile memory applications. For PZT/SIO, the relatively soft DW and low switching field make them suitable for low voltage switching and possible negative capacitance applications.

b. Domain Wall Pinning Mechanisms

Next, we discuss the possible origins of the pinning disorder and mechanisms that affect the DW pinning energy. As our films possess smooth surface morphology with similar surface roughness, and are coherently strained to the STO substrates (Supplemental Fig. S1) [30], we can exclude the effects of surface roughness and grain boundary as the primary source of DW pinning. Our XRD studies show that the PZT films exhibit no appreciable structural change after TQ at up to T_{th} (Supplemental Fig. S2-S3) [30]. We thus rule out the structural change as the origin of the temperature-dependence of DW roughness. In previous studies, it has been shown that oxygen vacancies in ferroelectric perovskites tend to migrate to the DW [14, 15], and can act as RB disorders [21]. First-principles density-functional calculations show that the pinning energy of oxygen vacancy for the in-plane DW motion in $PbTiO_3$ is 76 - 97 meV [14], which is on the same of order of magnitude of our extracted U_{RB}. Cation vacancies in ferroelectric perovskites, on the other hand, facilitate easy domain wall motion and make the ferroelectric “soft” [15]. Since all samples exhibit square-shaped PFM switching hystereses with the coercive fields larger than 10^5

V/cm [Fig. 1(c) and Supplemental Section 2] [30], we can rule out the cation disorder as a major DW pinning source.

Considering that all three types of samples are affected by the same type of disorder, *i.e.*, oxygen vacancies, an interesting question then is what gives rise to the more than a factor of 2 variation in U_{RB}. For the three types of PZT films, the top surfaces are exposed to the ambient conditions and identical. The key difference between these samples is the bottom correlated oxide electrode, which can modify U_{RB} in PZT through several mechanisms. The first possible contribution is the existence of a built-in electric field due to the asymmetric electric boundary condition. For ferroelectric films in the ambient conditions, the surface bound charges are effectively screened by the mobile charges absorbed from the ambient [32, 39], while an incomplete screening of the depolarization field can arise due to the band alignment between the ferroelectric and the bottom oxide electrode. This effect can tilt the ferroelectric double-well energy profile, leading to the observed polarization asymmetry [16]. For a given type of disorder, such as the cation/oxygen vacancies, this field can either enhance or reduce the pinning potential depending on the polarization direction. To verify this scenario, we listed in Table 1 the work function mismatch $\Delta W = W_{\mathrm{PZT}} - W_{\mathrm{electrode}}$ for all three systems. The work functions are 5.2 ± 0.1 eV for PZT [40], 4.8 ± 0.1 eV for LSMO [36], 4.5 eV [37] for LNO, and 5.05 eV for SIO [38], corresponding to $\Delta W_{\mathrm{LNO}} \geq \Delta W_{\mathrm{LSMO}} > \Delta W_{\mathrm{SIO}}$. This relation does not agree with that of the extracted U_{RB}, *i.e.*, $U_{\mathrm{RB,LSMO}} > U_{\mathrm{RB,LNO}} > U_{\mathrm{RB,SIO}}$. We thus rule out the work function mismatch as a dominant factor causing the variation in DW pinning.

The second scenario involves the interfacial clamping effect. It has been shown that the strain imposed by the substrate clamping can lead to a self-bias internal field that can contribute to the polarization asymmetry [41]. However, the XRD *θ-2θ* scans reveal that all three types of PZT films are coherently strained with similar *c*-axis lattice constants (Supplemental Section 1) [30], so that strain alone cannot account for the difference in DW pinning. The interface clamping effect can also originate from the mismatch of local lattice distortion, which is manifested as the tilt/rotation of the oxygen octahedral. The lattice distortion can impose internal stress that suppresses the DW mobility [42], which affects the dynamics of DW trapping/de-trapping. Although the rotation of oxygen octahedra in oxide electrodes is constrained by STO at the interface, it recovers a couple of unit cells away from the substrate [43, 44]. It is thus possible for the 10 nm oxide electrodes to carry the characteristic bulk distortion and impose considerable clamping in the interfacial PZT layers. We thus use the tolerance factors of bulk LSMO (0.924) [45], LNO (0.94) [27], and SIO (0.9917) [46] as the gauge to assess the level of lattice mismatch at the interface with PZT, whose in-plane octahedral rotation is relatively small (tolerance factor of 1.008) [47]. This indicates that LSMO is the most distorted, while SIO is the closest to the cubic structure. It is natural to expect the DW in PZT/LSMO (PZT/SIO) is most (least) prone to disorder pinning due to interfacial clamping, which is in good agreement with the observed trend of U_{RB}.

The third possible mechanism is that the correlated oxide electrode can act as a reservoir of oxygen vacancies at the interface, which then imposes an external biasing field. It has been directly imaged that the oxygen vacancies in LSMO accumulated by ferroelectric polarization can migrate to the ferroelectric side at the interface [18], while the accumulation of interfacial oxygen vacancies is known to induce an interfacial pinning field that causes ferroelectric fatigue [48]. The oxygen vacancy migration energy barrier height is 0.3 eV for PZT [49], which is much smaller than those for $La_{1-x}Sr_xMnO_3$ (0.6-0.8 eV for $x = 0.2$-0.5) [50], LNO (1.24 eV) [51], and SIO (1.9 eV) [52]. The oxygen vacancy migration energy difference in the correlated oxide layers is in line with the trend of U_{RB}, suggesting the ability for the electrode layer to supply oxygen vacancies may also affect the DW pinning potential.

V. Summary

In conclusion, we examined the energy competition between disorder pinning and thermal fluctuation on the DW configuration in high-quality epitaxial PZT thin films, which reveals the critical role of the correlated oxide electrodes in determining the thermal stability and size scaling limit of nanoscale domain structures. Our study sheds light on the optimization of electrode choice for achieving high density, low power ferroelectric-based device applications.

Acknowledgment

The authors would like to thank Zhiyong Xiao for valuable discussions. This work was primarily supported by the U.S. Department of Energy (DOE), Office of Science, Basic Energy Sciences (BES), under Award No. DE-SC0016153 (PFM studies). The work by YH, LZ, and XC were supported by the Semiconductor Research Corporation (SRC) under GRC Task No. 2831.001 (deposition and structural characterization of oxide heterostructures). The research was performed, in part, in the Nebraska Nanoscale Facility: National Nanotechnology Coordinated Infrastructure and the Nebraska Center for Materials and Nanoscience, which are supported by NSF ECCS: 2025298, and the Nebraska Research Initiative.

References

[1] Y. Wang, A. Tagantsev, D. Damjanovic, and N. Setter, Giant domain wall contribution to the dielectric susceptibility in $BaTiO_3$ single crystals, Appl. Phy. Lett. **91**, 062905 (2007).

[2] R. K. Vasudevan, Y.-C. Chen, H.-H. Tai, N. Balke, P. Wu, S. Bhattacharya, L.-Q. Chen, Y.-H. Chu, I.-N. Lin, and S. V. Kalinin, Exploring topological defects in epitaxial BiFeO3 thin films, ACS Nano **5**, 879 (2011).

[3] J. Seidel, L. W. Martin, Q. He, Q. Zhan, Y. H. Chu, A. Rother, M. E. Hawkridge, P. Maksymovych, P. Yu, M. Gajek, N. Balke, S. V. Kalinin, S. Gemming, F. Wang, G. Catalan, J. F. Scott, N. A. Spaldin, J. Orenstein, and R. Ramesh, Conduction at domain walls in oxide multiferroics, Nat Mater **8**, 229 (2009).

[4] J. Guyonnet, I. Gaponenko, S. Gariglio, and P. Paruch, Conduction at Domain Walls in Insulating $Pb(Zr_{0.2}Ti_{0.8})O_3$ Thin Films, Adv Mater **23**, 5377 (2011).

[5] G. Catalan, J. Seidel, R. Ramesh, and J. F. Scott, Domain wall nanoelectronics, Rev. Mod. Phys. **84**, 119 (2012).

[6] S. Cherifi-Hertel, H. Bulou, R. Hertel, G. Taupier, K. D. H. Dorkenoo, C. Andreas, J. Guyonnet, I. Gaponenko, K. Gallo, and P. Paruch, Non-Ising and chiral ferroelectric domain walls revealed by nonlinear optical microscopy, Nature Communications **8**, 15768 (2017).

[7] D. Li, X. Huang, Z. Xiao, H. Chen, L. Zhang, Y. Hao, J. Song, D.-F. Shao, E. Y. Tsymbal, Y. Lu, and X. Hong, Polar coupling enabled nonlinear optical filtering at MoS_2/ferroelectric heterointerfaces, Nat Commun **11**, 1 (2020).

[8] J. Song, Y. Qi, Z. Xiao, S.-H. Kim, A. I. Kingon, A. M. Rappe, and X. Hong, Domain Wall Enabled Hysteresis-Free Steep Slope Switching in MoS_2 Transistors, arXiv preprint arXiv:.00113 (2019).

[9] P. Paruch, T. Giamarchi, and J.-M. Triscone, Domain wall roughness in epitaxial ferroelectric $PbZr_{0.2}Ti_{0.8}O_3$ thin films, Phys. Rev. Lett. **94**, 197601 (2005).

[10] E. Agoritsas, V. Lecomte, and T. Giamarchi, Temperature-induced crossovers in the static

roughness of a one-dimensional interface, Phys. Rev. B **82**, 184207 (2010).

[11] P. Lucke, M. Bayraktar, Y. A. Birkhölzer, M. Nematollahi, A. Yakshin, G. Rijnders, F. Bijkerk, and E. P. Houwman, Hysteresis, Loss and Nonlinearity in Epitaxial $PbZr_{0.55}Ti_{0.45}O_3$ Films: A Polarization Rotation Model, Advanced Functional Materials **30**, 2005397 (2020).

[12] T. Giamarchi, A. B. Kolton, and A. Rosso, in *Jamming, Yielding, and Irreversible Deformation in Condensed Matter*, edited by M. Miguel, and M. Rubi (Springer Berlin / Heidelberg, 2006), pp. 91.

[13] T. Emig, and T. Nattermann, Disorder driven roughening transitions of elastic manifolds and periodic elastic media, The European Physical Journal B-Condensed Matter Complex Systems **8**, 525 (1999).

[14] L. He, and D. Vanderbilt, First-principles study of oxygen-vacancy pinning of domain walls in $PbTiO_3$, Phys. Rev. B **68**, 134103 (2003).

[15] P. Panda, and B. J. F. Sahoo, PZT to lead free piezo ceramics: a review, **474**, 128 (2015).

[16] L. C. Tănase, L. E. Abramiuc, D. G. Popescu, A.-M. Trandafir, N. G. Apostol, I. C. Bucur, L. Hrib, L. Pintilie, I. Pasuk, and L. Trupină, Polarization orientation in lead zirconate titanate (001) thin films driven by the interface with the substrate, Phys. Rev. Applied **10**, 034020 (2018).

[17] C. Lichtensteiger, C. Weymann, S. Fernandez-Pena, P. Paruch, and J.-M. Triscone, Built-in voltage in thin ferroelectric $PbTiO_3$ films: the effect of electrostatic boundary conditions, New Journal of Physics **18**, 043030 (2016).

[18] Y. M. Kim, A. Morozovska, E. Eliseev, M. P. Oxley, R. Mishra, S. M. Selbach, T. Grande, S. T. Pantelides, S. V. Kalinin, and A. Y. Borisevich, Direct observation of ferroelectric field effect and vacancy-controlled screening at the $BiFeO_3/La_xSr_{1-x}MnO_3$ interface, Nature Materials **13**, 1019 (2014).

[19] L. Zhang, X. G. Chen, H. J. Gardner, M. A. Koten, J. E. Shield, and X. Hong, Effect of strain on ferroelectric field effect in strongly correlated oxide $Sm_{0.5}Nd_{0.5}NiO_3$, Applied Physics Letters **107**, 152906 (2015).

[20] M.-G. Han, M. S. J. Marshall, L. Wu, M. A. Schofield, T. Aoki, R. Twesten, J. Hoffman, F. J. Walker, C. H. Ahn, and Y. Zhu, Interface-induced nonswitchable domains in ferroelectric thin films, Nature Communications **5**, 4693 (2014).

[21] P. Paruch, A. B. Kolton, X. Hong, C. H. Ahn, and T. Giamarchi, Thermal quench effects on ferroelectric domain walls, Phys. Rev. B **85**, 214115 (2012).

[22] M. Dawber, K. M. Rabe, and J. F. Scott, Physics of thin-film ferroelectric oxides, Rev. Mod. Phys. **77**, 1083 (2005).

[23] C. A. F. Vaz, J. Hoffman, C. H. Anh, and R. Ramesh, Magnetoelectric Coupling Effects in Multiferroic Complex Oxide Composite Structures, Adv. Mater. **22**, 2900 (2010).

[24] X. Hong, Emerging ferroelectric transistors with nanoscale channel materials: the possibilities, the limitations, Journal of Physics: Condensed Matter **28**, 103003 (2016).

[25] M. Bibes, J. Villegas, and A. Barthelemy, Ultrathin oxide films and interfaces for electronics and spintronics, Adv. Phys. **60**, 5 (2011).

[26] L. Zhang, H. Gardner, X. Chen, V. Singh, and X. Hong, Strain induced modulation of the

correlated transport in epitaxial $Sm_{0.5}Nd_{0.5}NiO_3$ thin films, Journal of Physics: Condensed Matter **27**, 132201 (2015).

[27] S. Catalano, M. Gibert, J. Fowlie, J. Íñiguez, J. M. Triscone, and J. Kreisel, Rare-earth nickelatesRNiO_3: thin films and heterostructures, Reports on Progress in Physics **81**, 046501 (2018).

[28] L. Zhang, X. Jiang, X. Xu, and X. Hong, Abrupt enhancement of spin–orbit scattering time in ultrathin semimetallic SrIrO3 close to the metal–insulator transition, APL Materials **8**, 051108 (2020).

[29] X. G. Chen, X. Zhang, M. A. Koten, H. H. Chen, Z. Y. Xiao, L. Zhang, J. E. Shield, P. A. Dowben, and X. Hong, Interfacial Charge Engineering in Ferroelectric-Controlled Mott Transistors, Advanced Materials **29**, 1701385 (2017).

[30] See Supplemental Material at URL for the details of sample growth & characterization, and domain writing & imaging.

[31] P. Gao, C. T. Nelson, J. R. Jokisaari, Y. Zhang, S.-H. Baek, C. W. Bark, E. Wang, Y. Liu, J. Li, C.-B. Eom, and X. Pan, Direct Observations of Retention Failure in Ferroelectric Memories, Advanced Materials **24**, 1106 (2012).

[32] J. Song, Z. Xiao, B. Chen, S. Prockish, X. Chen, A. Rajapitamahuni, L. Zhang, J. Huang, and X. Hong, Enhanced piezoelectric response in hybrid lead halide perovskite thin films via interfacing with ferroelectric $PbZr_{0.2}Ti_{0.8}O_3$, ACS applied materials interfaces **10**, 19218 (2018).

[33] Z. Xiao, S. Poddar, S. Ducharme, and X. Hong, Domain wall roughness and creep in nanoscale crystalline ferroelectric polymers, Appl. Phy. Lett. **103**, 112903 (2013).

[34] Z. Xiao, J. Hamblin, S. Poddar, S. Ducharme, P. Paruch, and X. Hong, Effect of thermal annealing on ferroelectric domain structures in poly (vinylidene-fluoride-trifluorethylene) Langmuir-Blodgett thin films, Journal of Applied Physics **116**, 066819 (2014).

[35] N. Pertsev, V. Kukhar, H. Kohlstedt, and R. Waser, Phase diagrams and physical properties of single-domain epitaxial $Pb(Zr_{1-x}Ti_x)O_3$ thin films, Phys. Rev. B **67**, 054107 (2003).

[36] M. P. de Jong, V. Dediu, C. Taliani, and W. Salaneck, Electronic structure of $La_{0.7}Sr_{0.3}MnO_3$ thin films for hybrid organic/inorganic spintronics applications, Journal of Applied Physics **94**, 7292 (2003).

[37] T.-H. Yang, Y.-W. Harn, K.-C. Chiu, C.-L. Fan, and J.-M. Wu, Promising electron field emitters composed of conducting perovskite $LaNiO_3$ shells on ZnO nanorod arrays, Journal of Materials Chemistry **22**, 17071 (2012).

[38] S. Okamoto, J. Nichols, C. Sohn, S. Y. Kim, T. W. Noh, and H. N. Lee, Charge transfer in iridate-manganite superlattices, Nano Letters **17**, 2126 (2017).

[39] S. V. Kalinin, Y. Kim, D. D. Fong, and A. N. Morozovska, Surface-screening mechanisms in ferroelectric thin films and their effect on polarization dynamics and domain structures, Reports on Progress in Physics **81**, 036502 (2018).

[40] I. Pintilie, C. M. Teodorescu, C. Ghica, C. Chirila, A. G. Boni, L. Hrib, I. Pasuk, R. Negrea, N. Apostol, and L. Pintilie, Polarization-control of the potential barrier at the electrode interfaces in epitaxial ferroelectric thin films, ACS Applied Materials Interfaces **6**, 2929

(2014).

[41] M. Boota, E. P. Houwman, M. Dekkers, M. Nguyen, and G. Rijnders, Epitaxial $Pb(Mg_{1/3}Nb_{2/3})O_3$-$PbTiO_3$ (67/33) thin films with large tunable self-bias field controlled by a $PbZr_{1-x}Ti_xO_3$ interfacial layer, Appl. Phy. Lett. **104**, 182909 (2014).

[42] A. Pramanick, D. Damjanovic, J. C. Nino, and J. L. Jones, Subcoercive cyclic electrical loading of lead zirconate titanate ceramics I: nonlinearities and losses in the converse piezoelectric effect, Journal of the American Ceramic Society **92**, 2291 (2009).

[43] P. E. Evans, T. Komesu, L. Zhang, D.-F. Shao, A. J. Yost, S. Kumar, E. F. Schwier, K. Shimada, E. Y. Tsymbal, and X. Hong, Detection of decoupled surface and bulk states in epitaxial orthorhombic $SrIrO_3$ thin films, AIP Advances **10**, 045027 (2020).

[44] P. Schütz, D. Di Sante, L. Dudy, J. Gabel, M. Stübinger, M. Kamp, Y. Huang, M. Capone, M.-A. Husanu, and V. Strocov, Dimensionality-driven metal-insulator transition in spin-orbit-coupled $SrIrO_3$, Phys. Rev. Lett. **119**, 256404 (2017).

[45] X. Hong, J.-B. Yau, J. Hoffman, C. Ahn, Y. Bason, and L. Klein, Effect of electric field doping on the anisotropic magnetoresistance in doped manganites, Phys. Rev. B **74**, 174406 (2006).

[46] A. G. Zaitsev, A. Beck, A. K. Jaiswal, R. Singh, R. Schneider, M. Le Tacon, and D. Fuchs, Anomalous pressure dependence of the electronic transport and anisotropy in $SrIrO_3$ films, Journal of Physics: Condensed Matter **32**, 345601 (2020).

[47] G. Rossetti, Structure and bonding in $PbZrO_3$–$PbTiO_3$ (PZT) alloys, British Ceramic Transactions **103**, 83 (2004).

[48] H. Al-Shareef, B. Tuttle, W. Warren, T. Headley, D. Dimos, J. Voigt, and R. Nasby, Effect of B-site cation stoichiometry on electrical fatigue of $RuO_2//Pb(Zr_xTi_{1-x})O_3//RuO_2$ capacitors, Journal of Applied Physics **79**, 1013 (1996).

[49] M. V. Raymond, and D. M. Smyth, Defects and charge transport in perovskite ferroelectrics, Journal of Physics and Chemistry of Solids **57**, 1507 (1996).

[50] N. Lee, Y. Lansac, H. Hwang, and Y. H. Jang, Switching mechanism of $Al/La_{1-x}Sr_xMnO_3$ resistance random access memory. I. Oxygen vacancy formation in perovskites, RSC advances **5**, 102772 (2015).

[51] A. Malashevich, and S. Ismail-Beigi, First-principles study of oxygen-deficient $LaNiO_3$ structures, Phys. Rev. B **92**, 144102 (2015).

[52] G. Wan, J. W. Freeland, J. Kloppenburg, G. Petretto, J. N. Nelson, D.-Y. Kuo, C.-J. Sun, J. Wen, J. T. Diulus, and G. Herman, Amorphization mechanism of $SrIrO_3$ electrocatalyst: How oxygen redox initiates ionic diffusion and structural reorganization, Science Advances **7**, eabc7323 (2021).

Captions:

FIG. 1. (a) Schematic experimental setup. (b-e) PFM characterizations of PZT/LSMO S1. (b) PFM amplitude and (c) phase switching hystereses. (d) PFM phase and (e) amplitude images of a domain structure written with $V_{\mathrm{bias}} = \pm 6\ V$. The lower panels show the signal profiles along the dashed lines. (f) $B(L)$ at RT for three PZT samples. The dash lines corresponds to fits $\propto L^{2\zeta}$ with $\zeta = 0.31$. Inset: Schematic of a rough DW.

FIG. 2. PFM phase images of the same stripe domains at selected TQ temperatures. (a) PZT/LSMO S2. (b) PZT/LNO. (c) PZT/SIO S1. The RT images were taken after 24 hours of initial writing. All images are shown at the same scale. The light (dark) color corresponds to the P_{up} (P_{down}) domains.

FIG. 3.(a-b) ζ *vs.* T obtained via *in situ* PFM imaging and the TQ method for (a) PZT/LSMO and (b) PZT/SIO. (c) ζ *vs.* T obtained via the TQ method for three types of PZT samples.

FIG. 4. Schematic of DW motion in a disordered energy landscape (a) without and (b) with an external field. The particle represents the pinned DW, which can hop to a new position via thermal activation. (c) Schematic $\zeta - T$ diagram. (d-f) ζ *vs.* T in log-log scale for (d) PZT/LSMO, (e) PZT/LNO, and (f) PZT/SIO.

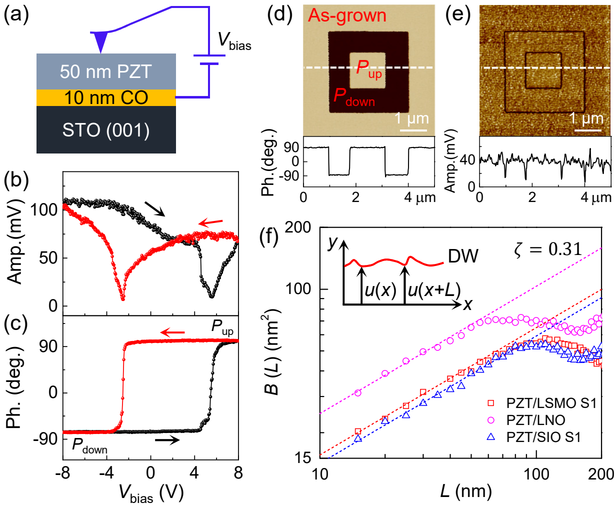
(a)
V_{bias}
50 nm PZT
10 nm CO
STO (001)
(b)
Amp.(mV)
100
50
0
(c)
Ph. (deg.)
90
0
-90
P_{up}
P_{down}
-8
-4
0
4
8
V_{bias} (V)
(d)
As-grown
P_{up}
P_{down}
1 μm
Ph.(deg.)
90
0
-90
0
2
4 μm
(e)
1 μm
Amp.(mV)
40
0
0
2
4 μm
(f)
200
100
15
y
DW
$u(x)$
$u(x+L)$
x
$\zeta = 0.31$
$B\,(L)$ (nm^2)
PZT/LSMO S1
PZT/LNO
PZT/SIO S1
10
100
200
L (nm)

(a) PZT/LSMO S2

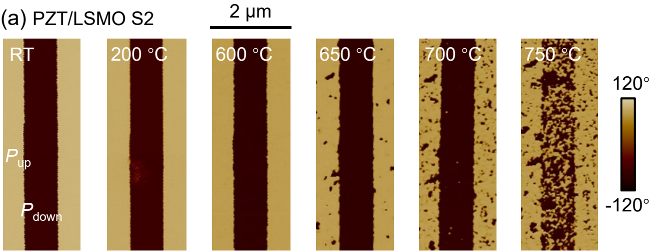

(b) PZT/LNO

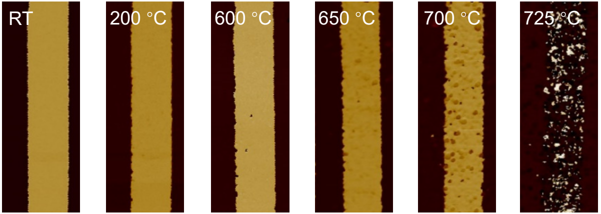

(c) PZT/SIO S1

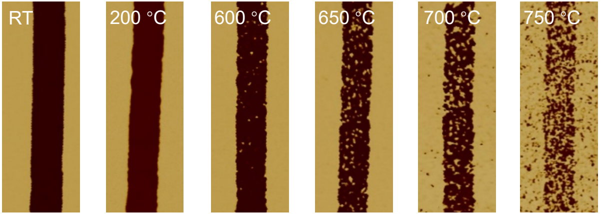

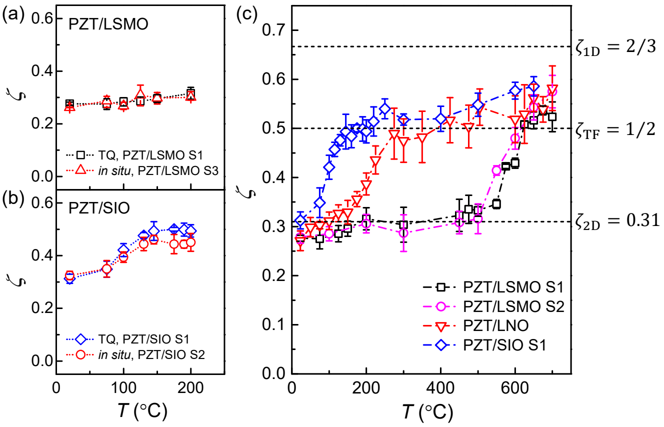
(a)
PZT/LSMO
0.6
0.4
0.2
0.0
ζ
TQ, PZT/LSMO S1
in situ, PZT/LSMO S3
(b)
PZT/SIO
0.6
0.4
0.2
0.0
ζ
TQ, PZT/SIO S1
in situ, PZT/SIO S2
0
50
100
150
200
T (°C)
(c)
0.7
0.6
0.5
0.4
0.3
0.2
0.1
0.0
ζ
$\zeta_{1D} = 2/3$
$\zeta_{TF} = 1/2$
$\zeta_{2D} = 0.31$
PZT/LSMO S1
PZT/LSMO S2
PZT/LNO
PZT/SIO S1
0
200
400
600
T (°C)

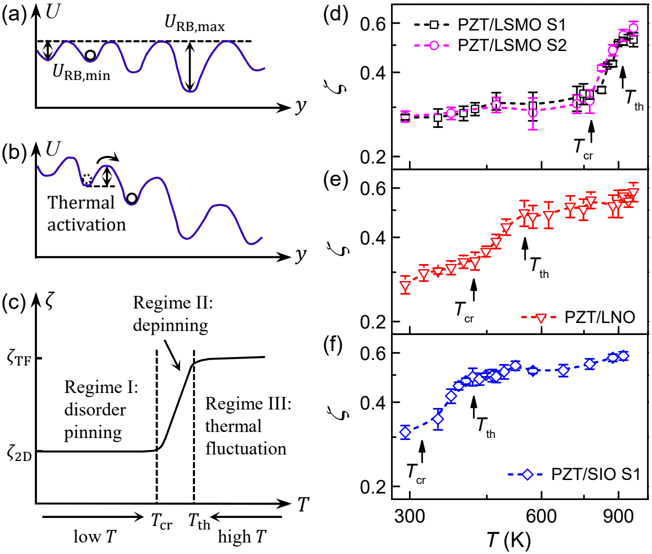
(a)
U
U_RB,max
U_RB,min
y
(b)
U
Thermal activation
y
(c)
ζ
ζ_TF
ζ_2D
Regime II: depinning
Regime I: disorder pinning
Regime III: thermal fluctuation
T
T_cr
T_th
low T
high T
(d)
PZT/LSMO S1
PZT/LSMO S2
T_th
T_cr
(e)
T_th
T_cr
PZT/LNO
(f)
T_th
T_cr
PZT/SIO S1
ζ
0.6
0.4
0.2
300
600
900
T (K)